

PAPER

Cite this: *Nanoscale*, 2022, **14**, 1421

A dynamic passive thermoregulation fabric using metallic microparticles†

Muluneh G. Abebe,^{id}*^a Gilles Rosolen,^a Jeremy Odent,^{id}^b Jean-Marie Raquez^{id}^b and Bjorn Maes^a

Maintaining comfort using photonic thermal management textiles has a large potential to decrease the energy cost for heating and cooling in residential and office buildings. We propose a thermoregulating fabric using metallic microparticles, which provides a dynamic and passive control of the infrared transmission, by adapting to the ambient temperature and humidity. The fabric is composed of tailored metal microparticles and a stimuli-responsive polymer actuator matrix, in order to benefit from strong scattering effects to control the wideband transmission of thermal radiation and to provide a sharp, dynamic response. The detailed numerical design demonstrates a wide dynamic ambient setpoint temperature window of ~ 8 °C, with the wearer staying comfortable in the range between 18 and 26 °C. Its compatibility for large-scale manufacturing, with a safe and strong thermoregulating performance indicates a vital energy-saving potential and paves the way to a more sustainable society.

Received 8th November 2021,
Accepted 19th December 2021

DOI: 10.1039/d1nr07390g

rsc.li/nanoscale

1. Introduction

At present, we continuously heat and cool large buildings in order to keep the occupants in thermal comfort, while there is no difference in energy consumption between a few or many occupants. Thus, a large amount of energy is wasted, activating an ongoing effort to reduce energy consumption.^{1,2} To this end, it is essential to localize the heating and cooling efforts, with solutions such as heated chairs, leg warmers, directed heating, and smart fabrics. In recent years, personal thermal management using smart fabrics enjoyed a rapid progress. To a large extent, the human body loses its metabolically generated heat by emitting infrared (IR) radiation centered near 10 μm .³ Therefore, fabric designs that capitalize on controlling radiative transfer became a research and industry target.

By implementing various photonic approaches, several state-of-the-art single mode (*i.e.*, cooling or heating) and dual-mode (heating^{4–7} and cooling^{8–11}), active and passive (requires no energy input) fabrics were designed and fabricated. Tong *et al.* conceived an Infrared Transparent Visible Opaque Fabric (ITVOF) for radiative cooling with an IR transparent textile, showing that a large (ideally total) hemispherical transmit-

tance grants the best performance for semitransparent fabrics.¹² On the other hand, Hsu *et al.* employed metallic nanowires with high IR reflectance for radiative heating.¹³ Further, Cai *et al.* used polyethylene alone, and combined with a metallic nano-mesh, to design cooling and heating fabrics, respectively.^{11,14} The crucial importance of the outer surface emissivity for thermoregulatory operation of an opaque fabric was pointed out.¹⁴

The most attractive smart fabrics are the ones that provide passive and dynamic radiative thermoregulating functionalities. These fabrics possess both cooling and heating modes, and switch between modes without external energy input.^{15,16} For example, Zhang *et al.* proposed carbon nanotube-coated bimorph fibers to dynamically modulate IR emissivity, providing both cooling and heating by adapting to the relative humidity.¹⁷ Furthermore, Hsu *et al.* reported a dual-mode textile, based on different emissivities of the outer fabric surface, so the clothes have to be inverted to switch between cooling and heating mode.¹⁸ In previous work, we proposed a Dynamic Transmittance Switch Textile (DTST), incorporating metal microfibrils with shape memory polymers to modulate the IR transmittance for both cooling and heating modes.¹⁹

Here, we demonstrate a promising framework for a metallic microparticle-based dynamic fabric (MMDF): a dynamic and passive thermal regulating fabric that controls the radiative transfer by adapting to the ambient temperature and humidity. We perform a comprehensive numerical study of the design's optical and thermal properties to determine optimized parameters for both heating and cooling functionalities. The dynamic switching is achieved *via* a shape memory polymer

^aMicro- and Nanophotonic Materials Group, Research Institute for Materials Science and Engineering, University of Mons, 20 Place du Parc, B-7000 Mons, Belgium.
E-mail: mulunehgeremew.abebe@umons.ac.be

^bLaboratory of Polymeric and Composite Materials, University of Mons, 20 Place du Parc, B-7000 Mons, Belgium

† Electronic supplementary information (ESI) available. See DOI: 10.1039/d1nr07390g

matrix that responds to environmental changes. The design capitalizes on the strong scattering properties of metallic microspheres, leading to a strong modulation of transmittance and reflectance as a function of the volume fraction. With thermal calculations, we reveal a significant 8 °C setpoint temperature window of the proposed fabric. Unlike (quasi-) ordered fabrics, the microparticles in this design are randomly distributed, and can be immersed in a relatively homogeneous polymer membrane, leading to feasible fabrication approaches.

The paper is structured as follows, in section 2 we present the working principle of the proposed technology. In section 3 we introduce the different modeling schemes: (1) the radiative properties of a single particle, (2) the properties of an embedded microparticle cloud, (3) the radiative transfer through the fabric, and (4) the analysis of total heat transfer. In section 4 we evaluate the fabric performance, and section 6 concludes.

2. Design working principle

Several daytime radiative cooling technologies utilize dispersed nano- to micro-scale particles in a polymer or other host matrix and substrate, which should be explored more for thermal textile designs.^{20,21} A technology with dispersed particles can be suitable for large-scale manufacturing of advanced textiles.^{22,23} Composite textiles incorporating dielectric microspheres have been reported for outdoor personal cooling,²³ as well as for indoor personal heating²⁴ functionalities.

Our proposed design (Fig. 1a) incorporates metallic microparticles in a stimuli-responsive shape-memory polymer

(SMP). These polymers are materials that can vary their shape from a temporary shape to a permanent shape upon exposure to an external stimulus such as heat, light, moisture, or magnetic field.²⁵ For the MMDF design, we propose temperature-responsive SMPs, due to their ability to respond to an ambient temperature change. More specifically, for our application the most interesting SMPs have permanent domains made of chemical crosslinks, and switching domains associated with either a glass transition or a melting point temperature.^{26,27} Temperature-responsive SMPs are typically deformed above T_{trans} , they remain fixed in this temporary, deformed shape when cooled below T_{trans} , and finally recover their original shape (before deformation) when heated again above T_{trans} . The shape recovery is thought to be due to the entropic relaxation of the polymer chains.

The MMDF design operation relies on two concepts: the strong scattering of micro-scale metallic particles in the IR, and the swelling and shrinking capabilities of specific polymers as a function of temperature or humidity.²⁸ Similar to previous dynamic functionalities, the design is flexible enough to deliver two operation modes: a cooling mode (when the ambient temperature is large) and a heating mode (for lower ambient temperatures).

For the heating mode, at lower temperatures, the polymer matrix shrinks [Fig. 1a (I)], which increases the volume fraction (f_v) of the particles, leading to increased scattering and reflectance. This directly blocks the radiative heat flux emitted from the human body to the ambient, leading to enhanced thermal comfort at low temperatures. On the other hand, for the cooling mode, at higher temperatures, expanding the polymer matrix [Fig. 1a (II)] decreases the particle volume fraction, scattering and reflectance, so the radiative heat flux of the body

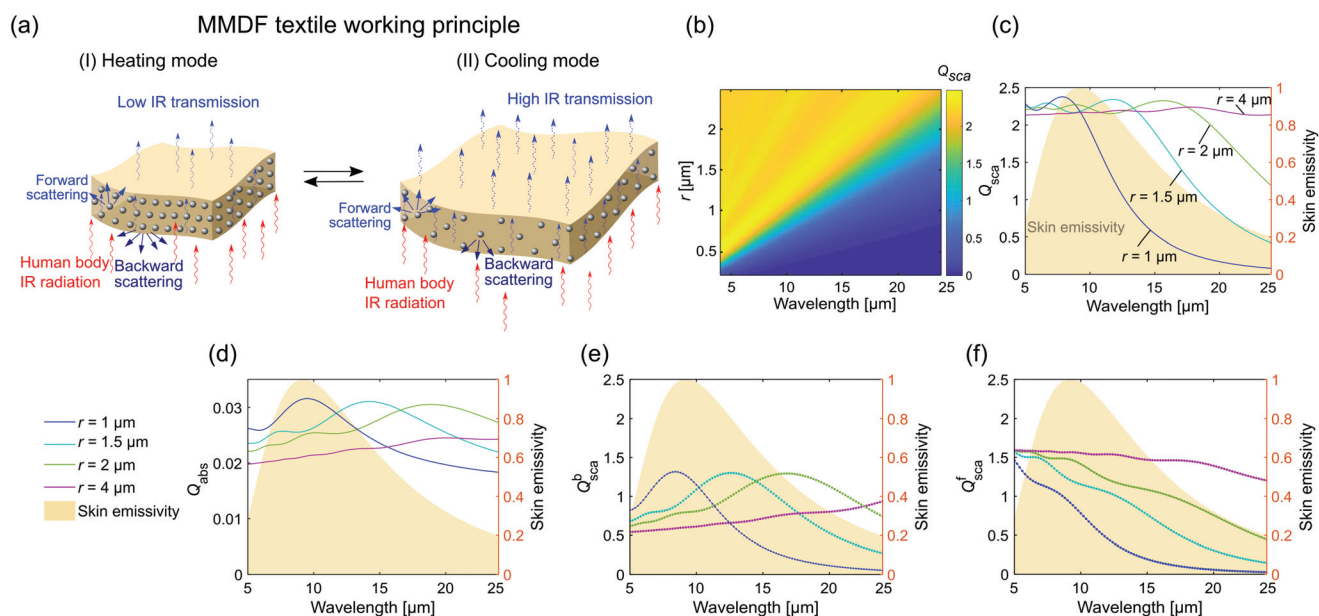


Fig. 1 (a) Schematic illustration of MMDF working principle with two-mode operation: (I) heating and (II) cooling. (b) Single silver microsphere Q_{sca} as a function of radius r and wavelength. (c) Q_{sca} , (d) Q_{abs} , (e) Q_{sca}^b , and (f) Q_{sca}^f as a function of wavelength for various radii r .

escapes to the ambient, leading to enhanced comfort at higher temperatures.

3. Modeling

The proposed principle provides comfort over a large temperature range (called the setpoint temperature window), when the parameters are chosen judiciously. To determine this temperature window, we need to implement multiple simulation steps (see Fig. S1 in ESI†) that build on each other, explained in the following sections.

First, in section 1, we use electromagnetic wave theory (*i.e.*, extended Lorenz–Mie solutions) to calculate the optical properties of a single metallic microsphere, which includes scattering Q_{sca} (both forward $Q_{\text{sca}}^{\text{f}}$ and backward $Q_{\text{sca}}^{\text{b}}$), extinction Q_{ext} , and absorption Q_{abs} efficiencies, and scattering phase function $\Phi(\theta)$, where scattering angle θ is the angle between the incident Ω' and scattered Ω directions. Second, in section 2, we study the effective radiative properties of a microsphere cloud uniformly dispersed in a polymer matrix (such as asymmetry factor g , scattering albedo ω_0 , effective absorption κ_{eff} , scattering σ_{eff} , and extinction β_{eff} coefficients). Third, in section 3, we investigate the radiative transfer analysis of a semitransparent particulate medium using a collision-based forward Monte Carlo method (with the effective properties from the previous step). Finally, in section 4, we utilize a heat balance analysis to study thermal transport through the fabric, leading to the ambient setpoint temperature.

The implemented methods have a good accuracy and require a much smaller computational cost compared to solving Maxwell's equations directly. However, we note that the independent scattering approach is used, so scattering is incoherent, and the microspheres are not in each other's near-field.^{29,30} Interestingly, the design requires only small volume fractions, which is suited for the independent scattering approach. In fact, a small fraction of particles is useful for other properties, such as the flexibility of the fabric.

3.1. Single particle properties

Studying the radiative properties of embedded nano- and microparticles is important for various disciplines (*i.e.*, aerospace, biomedical, photonics, and so on). For these materials, the fundamental electromagnetic approach is the Lorenz–Mie theory or an extended form, for example with applications in composite coatings such as polymers with dielectric hollow microspheres for thermal applications.^{31,32}

The simplest situation involves a non-absorbing embedding medium, so conventional Lorenz–Mie theory applies. On the other hand, when the medium is absorbing, it is customary to implement a direct addition of microsphere and medium absorption to determine the overall absorption. However, this ignores the microsphere's influence on the medium absorption, introducing inaccuracies in certain situations.

Therefore, here we implement the Generalized Lorenz–Mie extension formalism using the far-field (FF) method for a

microsphere in an absorbing medium, which is proven appropriate for radiative transfer in thermal applications.³³ Indeed, for a medium with very low or no absorption, the FF method gives the same results as the conventional Lorenz–Mie theory (detailed in the ESI†). By utilizing the FF method, we have the flexibility to introduce an absorbing matrix at a later stage.

The fabric modulates the composite's reflection/transmission, which is fundamentally related to a single microsphere's scattering properties. One has to choose the optimal microsphere size with a desired large scattering efficiency over the human body emission wavelength range. We use silver particles, with bulk refractive index data,³⁴ which has a low absorption in the mid-IR region. Here, it is assumed that the optical constant of the particle is not influenced by size. For the medium we employ an ideal polymer with real index $n_{\text{m}} = 1.5$.

Fig. 1b shows the scattering efficiency as a function of particle radius r and wavelength in the mid-IR region. One observes weak scattering for smaller microspheres ($r < 300$ nm) over the human body emission wavelength range (5–25 μm), but the scattering increases towards smaller wavelengths as resonances appear (yellow bands).

The details are visible in Fig. 1c. At a constant radius and for decreasing wavelength, the scattering increases towards a large maximum (*e.g.*, maximum at 12 μm for radius 1.5 μm), and then oscillates towards smaller wavelengths. Metallic spheres with a radius of about 1.5 μm are very interesting, as the maximum is large, and the scattering is fairly broad, covering well the human emission range. Indeed, smaller radii lead to narrower spectra (blue curve for $r = 1$ μm in Fig. 1c), whereas larger radii lead to slightly lower maxima (green curve for $r = 2$ μm in Fig. 1c).

In general, we observe large scattering efficiencies, with Q_{sca} above 2, and furthermore the absorption is negligible (see Fig. 1d and Fig. S2a in ESI†). This is typical for metals in the mid and far-IR, as the free electrons lead to a Drude model with a very large and negative permittivity for these small frequencies and a relatively small imaginary part of the permittivity (leading to weak absorption).^{35,36}

A further argument to choose a reference radius of 1.5 μm for further modeling is offered by the backward and forward scattering efficiencies (Fig. 1e and f, respectively). Both characteristics are favorable for 1.5 μm , as $Q_{\text{sca}}^{\text{hrmb}}$ peaks around 10–15 μm , and $Q_{\text{sca}}^{\text{f}}$ is fairly broadband. Higher radii have a stronger $Q_{\text{sca}}^{\text{f}}$, but their $Q_{\text{sca}}^{\text{b}}$ is less pronounced in the body emission range. This backward scattering leads to an optimal cloud reflection/transmission with the $r = 1.5$ μm radius particles (see Fig. S2b–i in ESI†).

3.2. Embedded microparticle cloud

Now we study the radiative properties of an ensemble randomly dispersed in a polymer matrix. For independent scattering, with N_i the number of microspheres (with radius r_i) per unit volume (*i.e.*, $f_{v,i} = 4/3\pi r_i^3 N_i$), the fraction of energy scattered by all the microspheres (per unit length along the direction of the incoming electromagnetic wave) is equal to the

scattering cross section summed over all microspheres.²⁹ Thus, one obtains the effective scattering coefficient:

$$\sigma_{\text{eff}} = \sum_{i=1}^m N_i C_{\text{sca},i} = \sum_{i=1}^m \frac{3f_{v,i}}{4r_i} Q_{\text{sca},i}, \quad (1)$$

the effective absorption coefficient:

$$\kappa_{\text{eff}} = \sum_{i=1}^m N_i C_{\text{abs},i} + \kappa_m = \sum_{i=1}^m \frac{3f_{v,i}}{4r_i} Q_{\text{abs},i} + \frac{4\pi k_m}{\lambda}, \quad (2)$$

and the effective extinction coefficient:

$$\beta_{\text{eff}} = \sum_{i=1}^m N_i C_{\text{ext},i} = \sum_{i=1}^m \frac{3f_{v,i}}{4r_i} Q_{\text{ext},i}, \quad (3)$$

with the scattering albedo $\omega_0 = \sigma_{\text{eff}}/\beta_{\text{eff}}$. $C_{\text{sca},i}$, $C_{\text{abs},i}$, and $C_{\text{ext},i}$ are the scattering, absorption, and extinction cross sections. The absorption in the polymer matrix is calculated as $\kappa_m = 4\pi k_m/\lambda$ using the complex refractive index k_m . The expressions can be used for several types of inclusions, indexed by i , but here we use uniform Ag microspheres with $r = 1.5 \mu\text{m}$, so the summations disappear.

Fig. 2a–c shows the calculated σ_{eff} , κ_{eff} , and β_{eff} as a function of f_v and wavelength. As expected, the σ_{eff} increases with f_v (near the relevant $10 \mu\text{m}$ wavelength), showing a potential for dynamic modulation. This stems from the large Q_{sca} of a single Ag microsphere in the same wavelength region (see Fig. 1c). Overall, the effective absorption efficiency of the fabric is very low, but shows a rapid increase when f_v surpasses 0.03. This indicates a possible absorption in the fabric in heating mode (at high f_v). Similarly, the extinction β_{eff} also increases with f_v .

Because $\Phi(\theta)$ (the directional distribution of scattered energy) is the same for each microsphere (for a uniform blend), it is also valid for the particle cloud.²⁹ Similarly, the asymmetry factor g of the ensemble is the same for the microspheres, defined as

$$g = \frac{1}{4\pi} \int_{4\pi} \Phi(\theta) \cos(\theta) d\Omega. \quad (4)$$

When g is greater than 0, forward scattering is larger than backward scattering, and *vice versa* (see Fig. 2d, $g > 0$ for wavelength less than $10 \mu\text{m}$). In the case of isotropic scattering g is

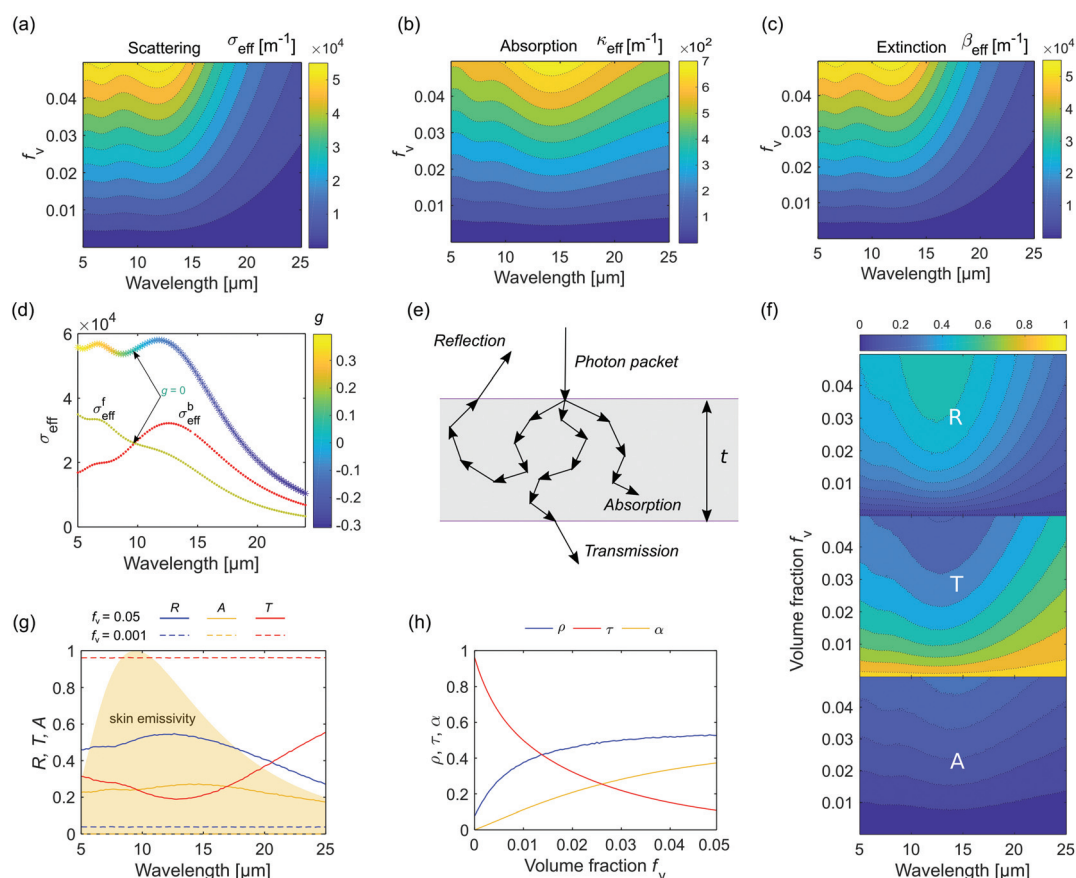


Fig. 2 Microsphere ensemble effective (a) scattering σ_{eff} , (b) absorption κ_{eff} , and (c) extinction β_{eff} coefficients. (d) σ_{eff} and asymmetry factor g , with forward and back scattering coefficients (σ_{eff}^f , σ_{eff}^b) for $f_v = 0.05$. (e) Schematic illustration of radiative transport through a slab with thickness t . (f) Spectral reflectance R , transmittance T and absorptance A as a function of wavelength and f_v . (g) R , T , and A as a function of wavelength for $f_v = 0.05$ and $0.005 \mu\text{m}$, with the human body emissivity at a skin temperature of $34 \text{ }^\circ\text{C}$. (h) Spectrally integrated reflectance ρ , transmittance τ , and absorptance α as a function of f_v for $t = 150 \mu\text{m}$.

zero. We compute the effective backward $\sigma_{\text{eff}}^{\text{b}}$ and forward $\sigma_{\text{eff}}^{\text{f}}$ scattering coefficients directly from the single particle $Q_{\text{sca}}^{\text{b}}$ and $Q_{\text{sca}}^{\text{f}}$ (Fig. 1e and f) using incoherent summation rules for $f_v = 0.05$ (see Fig. 2d), which leads to the total scattering coefficient $\sigma_{\text{eff}} = \sigma_{\text{eff}}^{\text{f}} + \sigma_{\text{eff}}^{\text{b}}$. When $\sigma_{\text{eff}}^{\text{b}}$ is higher than $\sigma_{\text{eff}}^{\text{f}}$, g is negative (and *vice versa*). At the point where $\sigma_{\text{eff}}^{\text{b}} = \sigma_{\text{eff}}^{\text{f}}$ (around 10 μm), g is zero and scattering into the forward and backward hemispheres are equal.

3.3. Radiative transport analysis

Radiative transport through the fabric is modeled using the conventional radiative transfer equation (RTE). We consider the fabric as a homogeneous slab medium (see Fig. 2e), and employ the effective radiative quantities computed in the previous section as an input to solve the RTE. Subsequently, the fabric's overall radiative transport qualities (*i.e.*, transmission, reflection, absorption) in the human body emission band are retrieved, which are crucial for the thermal model in the next section.

The RTE in a participating medium is written as

$$\frac{dI}{ds} = \kappa_{\text{eff}} I_{\text{bb}} - \beta_{\text{eff}} I + \frac{\sigma_{\text{eff}}}{4\pi} \int I \Phi(\Omega', \Omega) d\Omega', \quad (5)$$

with I the radiative intensity field, s the path length, I_{bb} the blackbody intensity, and $\Phi(\Omega', \Omega)$ the scattering phase function, which describes the distribution of scattered energy coming from direction Ω' into direction Ω with the scattering angle θ between the two directions.^{29,37} The first term on the right-hand side represents the emission, the second term represents extinction due to absorption and scattering, the last term denotes radiation augmentation due to in-scattering.

The RTE can be solved using various analytical and numerical methods (*i.e.*, Four-Flux, Two-Flux, P1 approximation, discrete ordinate, finite element...).^{29,37} Due to its accuracy and simplicity, the Monte Carlo (MC) method is chosen for this study. We implement the collision-based forward MC method, extending and adopting a validated algorithm used by Yalçın *et al.* in various works.^{38,39} This algorithm's main advantage is to capitalize on the parallelization possibility and to utilize a GPU accelerator, allowing to launch tens of thousands of photons and to retrieve results in reasonably short times.

The comprehensive MC implementation for solving the RTE can be found in ref. 37 and 40. The flow chart and detailed description are in the ESI.† Overall, a photon is launched at the upper boundary of the fabric for each run, with a certain propagation direction. The photon moves until it is reflected by or transmitted through the fabric (see Fig. 2e). During each step the photon travels a random distance with mean equal to the photon's path-length in the medium. When scattering occurs, the new propagation direction is determined *via* the Henyey–Greenstein scattering phase function, which approximates the exact phase function from the Mie solution, thus simplifying the computational task.^{29,41} The Henyey–Greenstein phase function utilizes the asymmetry factor g calculated in the previous section.

When photons strike the fabric interface, a fraction of them will be reflected, and the rest will be refracted. The entrance angle for photon tracing is handled using Snell's law. Specular reflectance at the boundaries is computed using conventional Fresnel equations,³⁷ combined with Maxwell–Garnett effective medium theory for the fabric's refractive index (detailed in the ESI.†).⁴² Thus, the surface reflection adapts to the volume fraction (f_v) modulation.

The important spectral hemispherical parameters retrieved from the RTE solution for fabric thickness $t = 150 \mu\text{m}$ are displayed in Fig. 2f as a function of f_v . The top panel presents the spectral hemispherical reflectance (R) of the fabric. R increases with f_v , especially for 7–15 μm where the human body emissivity is substantial, thus returning an important fraction of the body's radiation back to the skin. This mirrors the trend of σ_{meff} discussed previously (see Fig. 2a).

The middle panel shows the spectral hemispherical transmittance (T) through the fabric, which decreases with increasing f_v , so the fabric allows less thermal radiation to reach the ambient. This correlates with the large cloud effective extinction coefficient (β_{eff}) (see Fig. 2c). The bottom panel presents the spectral hemispherical absorptance (A) of the fabric, which is very low for small f_v , but increases rapidly after $f_v = 0.03$. This is connected with the behavior of κ_{eff} (see Fig. 2b), which is higher around 14–17 μm , and A shows the same trend.

As an important result, for $t = 150 \mu\text{m}$, Fig. 2g shows R , T , and A for two specific cases, $f_v = 0.001$ and 0.05, respectively, which we associate with the cooling and heating mode. In cooling mode ($f_v = 0.001$, dashed lines) we observe very low R and A , so the fabric is almost perfectly transparent for all wavelengths. In heating mode ($f_v = 0.05$, solid lines) R and A are significant, and decrease somewhat above 15 μm , while T is low for the important 9–16 μm region.

For the heat transfer analysis, one needs the total radiative quantities, which are the spectrally integrated R , T , and A , weighted by the Planck distribution (with a 34 °C skin temperature). Thus, the total reflectance (ρ), transmittance (τ), and absorptance (α) indicate how much body emission is reflected, transmitted, and absorbed/emitted by the fabric (see Fig. 2h for $t = 150 \mu\text{m}$). This result is fundamental to the dynamic functionality: as a function of the volume fraction these parameters are drastically adjusted, leading to a cooling or heating effect.

3.4. Heat transfer model

The fabric's overall performance is understood by modeling the heat transfer from the skin to the ambient. The main objective is to determine the maximum and minimum surrounding environment temperature, which the proposed fabric can maintain without affecting the wearer's thermal comfort: the setpoint temperature window. We consider a dry condition, with negligible moisture transfer. Radiative and conductive processes constitute the heat transfer through the air gap and the fabric, while the heat dissipation from the fabric to the ambient is *via* radiation and convection. We model the fabric as a semitransparent layer (keeping the radiative properties in

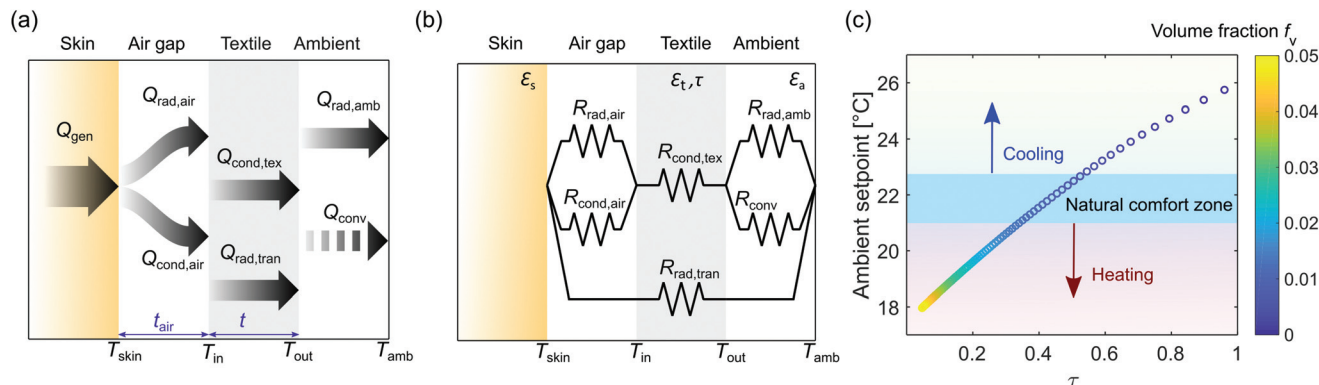


Fig. 3 (a) The main heat flow channels when the fabric covers skin, with an air gap in between. (b) Thermal circuit analogy. (c) Ambient setpoint temperature as a function of transmittance τ and f_v , for $t = 150 \mu\text{m}$. The natural comfort zone, setpoint window for cooling and heating are indicated.

mind), such that it handles the two proposed cases, opacity and near-complete transparency. A 1D steady-state heat transfer analysis (see Fig. 3a and b) is implemented to determine the temperature window as a function of the radiative parameters (detailed in the ESI†).

The requirement for a wearer's thermal comfort is the equality between metabolic heat generation (Q_{gen}) and total heat loss in dry condition (Q_{dry}). The total heat loss is controlled by the effective heat transfer coefficient h_{eff} , which is inversely related to the effective thermal resistance R_{eff} between skin and ambient ($R_{\text{eff}} = h_{\text{eff}}^{-1}$). The dynamic functionality modulates R_{eff} for heating and cooling modes accordingly. The total heat flux through air gap and fabric to the ambient (in dry condition) is given by

$$Q_{\text{dry}} = h_{\text{eff}}(T_{\text{skin}} - T_{\text{amb}}), \quad (6)$$

with T_{skin} and T_{amb} the skin and ambient temperature.

We assume a constant $Q_{\text{gen}} = 70 \text{ W m}^{-2}$, corresponding to a sedentary individual with a skin temperature of $34 \text{ }^\circ\text{C}$.⁹ The emissivity of the skin is approximated as a gray body with $\epsilon_{\text{skin}} = 0.98$ (ref. 43) and the emissivity of ambient as a black body is $\epsilon_{\text{amb}} = 1$. For the micro-climate, an air gap thickness of 2.5 mm is used. We consider the thermal conductivity of air $k_{\text{air}}(T)$ to be a function of local temperature, obtained by fitting data using a fourth-order polynomial (detailed in the ESI†).⁴⁴ The effective thermal conductivity of the fabric k_{MMDF} is calculated using classical effective medium theory depending on f_v .^{45,46} The natural convection heat transfer coefficient $h = 3 \text{ W m}^{-1} \text{ K}^{-1}$ allows to investigate air circulation of the surrounding environment. Convective heat transfer in the air gap is negligible due to the small Rayleigh number, which stems from the relatively small air gap thickness.

A typical setpoint temperature band for human thermal comfort in buildings, especially in offices, is subjective and requires polls and statistics, thus we consider a general average of $21\text{--}23 \text{ }^\circ\text{C}$ natural comfort zone for traditional textiles.^{47,48} A lower setpoint corresponds to a better fabric heating performance, and a higher setpoint corresponds to a

better cooling performance. Simulated setpoint temperature for a specific case with $h = 3 \text{ W m}^{-1} \text{ K}^{-1}$, $t = 150 \mu\text{m}$, $t_{\text{air}} = 2.5 \text{ mm}$ is presented in Fig. 3c as a function of f_v and τ .

As can be observed, the proposed fabric provides a large setpoint window of around $8 \text{ }^\circ\text{C}$, thus an expanded thermal comfort range with the lowest setpoint of $18 \text{ }^\circ\text{C}$, and the highest setpoint of $26 \text{ }^\circ\text{C}$ is achievable. The lowest setpoint corresponds to τ close to 0.1, where $f_v = 0.05$, which is an estimated maximum shrinking limit of a polymer matrix, so the fabric is quite opaque to thermal radiation emitted by the human body. On the other hand, the highest setpoint corresponds to $\tau = 0.96$, where $f_v < 0.001$ (expected maximum expansion of a polymer matrix), hence the fabric is highly transparent to the body thermal radiation.

Compared to the natural comfort zone using a traditional static fabric, the highest setpoint is $3 \text{ }^\circ\text{C}$ more than the upper bound ($23 \text{ }^\circ\text{C}$), and the lowest setpoint is $3 \text{ }^\circ\text{C}$ less than the lower bound ($21 \text{ }^\circ\text{C}$). This is a very wide setpoint window, see the literature comparison in ref. 19. Thus, the proposed fabric demonstrates both superior cooling and heating functionalities to preserve the wearer's thermal comfort in a highly dynamic temperature situation.

4. Performance considerations

This section analyzes the influence of various factors affecting the performance. Heat transfer in clothing systems is complex and strongly related to parameters such as fabric thickness, air gap thickness, material properties, fabrication, and so on, which we investigate here.

From the literature concerning smart fabrics, the thickness of most technologies is in the range of $50\text{--}250 \mu\text{m}$, so we examine ρ , τ , and α for various thicknesses ($50\text{--}200 \mu\text{m}$), see Fig. 4a–c. The corresponding ambient setpoint temperatures are depicted in Fig. 4d, as a function of f_v and τ .

The thin design shows the smallest window (the range between cooling and heating), and with increasing thickness, a larger window is acquired. Furthermore, the thin fabric

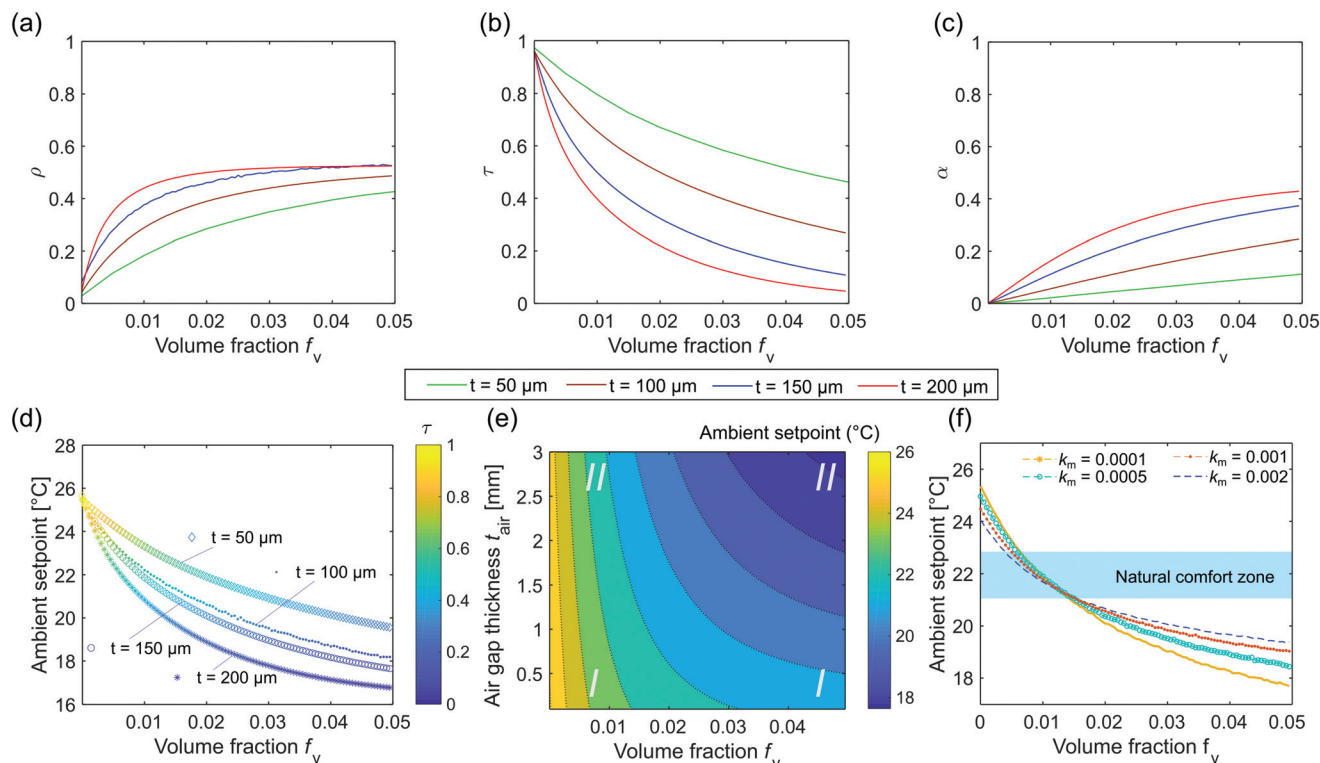


Fig. 4 (a) ρ , (b) τ , and (c) α as a function of f_v for various thicknesses t . (d) Ambient setpoint temperature as a function of f_v and τ for various thicknesses t . (e) Map of ambient setpoint temperature as a function of t_{air} and f_v . (f) Ambient setpoint temperature as a function of f_v for various absorption levels in the matrix ($k_m = 0.0001, 0.0005, 0.001$, and 0.002).

shows a nearly linear trend, while the thicker one is more curved. Finally, the lower setpoint is much more variable than the upper one.

Following an increase in f_v , ρ first increases rapidly and saturates (Fig. 4a), while τ decreases continuously due to the continuous increase of α (Fig. 4b and c). Thus, at constant f_v , increasing thickness directly increases the absorption, thus decreasing the transmission even for small f_v , resulting in the setpoint curve's parabolic shape (Fig. 4d). Interestingly, this explains the small variability in the upper setpoint and the larger variability of the lowest setpoint as a function of fabric thickness.

For example, $t = 200 \mu\text{m}$ demonstrates the lowest setpoint temperature due to increased α , and thus increases emission (ϵ) via Kirchhoff's law. Indeed, α/ϵ transports radiation to both sides (*i.e.*, to ambient and to the skin) of the fabric. On the other hand, ρ and τ completely reverse the radiative transport (to skin or ambient), thus, increasing α helps the heating process by returning heat back to the skin.

Overall, even though the larger thickness shows a significantly lower setpoint temperature, the larger volume is more difficult for mechanical actuation of the polymer, and the flexibility of the fabric decreases. It is also preferable to keep the thickness small to avoid unnecessary absorption in the cooling mode. Even the most highly IR transparent polymer possesses inherent absorption due to hydrogen–oxygen bonds that could result in small absorption. Furthermore, to

ensure lateral shrinking and expansion, a smaller thickness is desirable.

The effect of air gap thickness is illustrated in Fig. 4e. One can distinguish two regions for each mode (cooling and heating). For cooling mode (small f_v), in the bottom-left corner (I), we have an improved highest upper-bound ambient setpoint temperature because the conductive heat transfer is dominant due to lower insulation (reduced thermal resistance) offered by the reduced air gap. In the top-left corner (II), the upper-bound ambient setpoint has decreased (compared to region I) due to an increase in thermal resistance as the air gap increases (reducing conduction from skin to fabric).

For heating mode (large f_v), in the bottom-right corner (I), we observe a moderate lower-bound setpoint because of lower thermal resistance due to a small air gap. In the top-right corner (II), we see a reduced lower-bound setpoint due to substantial insulation provided by the increased air gap (*i.e.*, reduced thermal conduction).

Overall, it is clear that region (I) in cooling mode (tight-fitting clothing, small f_v) and region (II) in heating mode (loose-fitting clothing, large f_v) provide the best performance. However, for a dynamic fabric, one chooses a preferable fixed air gap, which results in both desirable upper and lower bounds. Here, $t_{\text{air}} = 2.5 \text{ mm}$ shows promise for both upper and lower bound setpoint temperatures. Furthermore, the ambient airflow is investigated by varying the convective heat transfer coefficient h (see Fig. S5a, ESI†). The influence of considering a gray body

assumption for the ambient (*e.g.*, $\epsilon_a = 0.9$) has a minimal effect on the performance of the MMDF (Fig. S5b, ESI†).

For the matrix, various shape memory polymers have been successfully synthesized, mainly based on polyurethane,⁴⁹ styrene,⁵⁰ cyanate ester,⁵¹ and polyamide.⁵² Recent studies have reported that polymers such as bio-based polylactide-urethane and polyurethane show programmable shape-memory properties around the human body temperature, as well as lower absorption in the thermal band.^{53,54} For example, Shua *et al.* show high transmission of biodegradable polyurethane.⁵⁴ Leng *et al.* studies styrene-based shape memory polymers with very low absorption ($\alpha = 0.03$) in the human body emission wavelength range.⁵⁵ However, due to inherent refractive index and absorption coefficient variability, hydrogel-based thermoresponsive polymers are not suitable for MMDF operation.^{56,57}

For example, polymer-based materials, including SMPs, have a limitation in the attainable contrast of the refractive index, because most polymers have a refractive index between 1.4 and 1.7 in the visible and IR regime. The optical absorption properties of thermoresponsive, and indeed of many other stimuli-responsive polymers in the IR, are significantly sample dependent. This is due to the particular manufacturing process used or the presence of impurities such as antioxidants, heavy-metal salts, or oxides as residues of the catalysts used in polymerization and water microdroplets. Similarly, exposure of the material to environmental factors such as high temperatures, ultraviolet radiation, mechanical stress, and high-energy irradiation can significantly change the material's IR optical constants. Therefore, it is difficult to propose a unique set of intrinsic optical constants for the matrix.

Consequently, we introduce a non-dispersive absorbing medium, in order to understand the effect of polymer matrix absorption on the overall performance. We calculate the setpoint temperature (for $t = 150 \mu\text{m}$) using various values of a constant absorption index of the matrix (k_m from 0.0001 to 0.002), see Fig. 4f. As expected, the setpoint temperature for both cooling and heating mode varies. Interestingly, with high absorption ($k_m = 0.002$) the cooling (low f_c) remains 1°C above the upper natural setpoint, while the heating mode (high f_h) remains 1.6°C below the lower natural setpoint. Even though a careful selection of a (moderate to highly) IR-transparent polymer matrix is necessary for an exceptional performance, the design is capable of delivering adequate temperature regulation (a minimum setpoint window of 4.6°C) using an absorbing polymer.

For the microspheres, various metals can be used. For example, we compare the radiative response of silver (Ag), copper (Cu), gold (Au), and aluminum (Al) microspheres (see Fig. S6 in ESI†). As expected, most metals show a similar response in the IR region and, thus can be used for the textile. However, due to the inherent antimicrobial properties of Ag and Cu, they may be a favorable design choice.^{58,59}

On the other hand, one can utilize a microsphere composed of a dielectric core and a thin metal shell. We performed electromagnetic calculations using extended Lorenz–Mie solu-

tions for Ag-coated dielectric spheres (silicon dioxide, zinc oxide, and titanium dioxide). Results indicate that the radiative response of such microspheres (independent of the material used as a dielectric core) is similar to the solid-metal spheres for a coating shell thickness of about 100 nm and above (see Fig. S7 in ESI†). The advantage of using such core–shell microspheres is to introduce fabrication flexibility for cost-effective large-scale manufacturing.

Several extrinsic synthesis/fabrication methods can be utilized to produce the envisioned MMDF textile. In extrinsic methods, microparticles are prepared separately and incorporated into the polymer matrix during processing.⁶⁰ By using kinetic dispersion approaches such as shear force or ultrasonic vibrations, particles are dispersed.⁶¹ Furthermore, the microsphere surfaces can be passivated to facilitate dispersion. Even though a uniform dispersion of particles is hard to achieve, a satisfactory uniformity can be acquired due to the design's small microsphere volume fraction requirement. For example, Cai *et al.* fabricated a zinc oxide–polyethylene (ZnO–PE) textile by mixing ZnO particles with melted PE at a specific weight ratio, followed by melt-pressing the composite mixture into a thin film. In this way, a uniformly distributed particle cloud in the whole volume with $150 \mu\text{m}$ thickness is achieved.²³ Typically, intrinsic methods deliver smaller nanoscale particles that are perhaps not ideal for the design proposed here.⁶²

5. Practical realization

Finally, to realize a practical textile, we explore potential modifications. Fabric breathability, water wicking, and vapor transmission have to be considered to avoid discomfort, *e.g.*, when sweating. A primary way to achieve these properties is to introduce interconnected nanopores within the fabric. See, *e.g.*, the well-known nano-PE (poly-ethylene) approach, which has been utilized effectively for cooling and heating fabrics, from lab-scale to large-scale production.^{9,14}

To explore this approach we perform calculations (Lorenz–Mie solutions and effective medium theory) to optimize the size and volume fraction of nanoholes so they do not affect the radiative response. Results show that nanoholes with a radius of about 250 nm (and below) will not affect the radiative response brought about by the metal microparticles (see Fig. S8, ESI†). Indeed, these pores are too small to interact with IR radiation, while they substantially scatter in the visible range (potentially adding to a visual opaqueness aspect). At the same time, these pores are far larger than water molecules, thus facilitating water vapor transmission. Furthermore, the overall fabric performance is not affected by the nanoholes when the volume fraction is 0.25 and below.

Considering the material cost, equipment availability, and production constraints, there are various techniques to introduce the nanoholes. Here we suggest a few widely used approaches: (1) using chemically synthesized nanoporous

shape memory polymers, which can be achieved by the combination of phase separation, crystallization, and cross-linking.^{63,64} (2) Introducing the nanoholes physically after the MMDF is fabricated, so one uses nano/micro-needles to mechanically punch holes into the membrane.^{14,18} (3) Using electrospinning, which produces fibrous membranes with controlled porosity, thickness, and potentially particle doping.^{65,66} (4) Using melt-extrusion to fabricate doped fibers, which can be carefully woven into a fabric, with a controlled porosity as presented in Fig. 5a.^{23,67}

Indeed, the last two methods are attractive for the textile industry as most fabrics are based on fibers and yarns. Thus, we assess in detail the MMDF fabric based on ordered fibers as well as randomly distributed fibers, and compare them with the corresponding membrane-based approach. First, we retrieve the effective dielectric permittivity and magnetic permeability of the composite (particles plus polymer) utilizing the so-called Maxwell–Garnet Mie (MGM) size-dependent effective medium theory (details in the ESI†).^{68–70} Second, we set up a fabric configuration with cylindrical fibers in both an ordered manner and a randomly distributed one, respectively. The effective permittivity and permeability retrieved from MGM calculations for a microsphere size of $r = 1.5 \mu\text{m}$ and volume fraction of 0.05 are used as input material property for the fibers. In both ordered and random situations, a fiber radius $r_f = 15 \mu\text{m}$, fiber volume fraction of 0.85, and fabric thickness $t = 150 \mu\text{m}$ are considered. The ordered fiber geometry is simulated using a commercial finite element solver (COMSOL Multiphysics), and the random geometry is computed using Monte Carlo methods (details in the ESI†).

The spectral reflectance (R) in the IR (5 to 25 μm) for membrane (blue), ordered fibers (light green), and random fibers (orange) are displayed in Fig. 5b, leading to an integrated reflectance of $\rho = 0.528$, 0.536, and 0.541, respectively. Furthermore, R for the random fibers increases with wavelength and starts to deviate slightly from the ordered configuration, while it differs a bit more from the membrane curve beyond 17 μm . This can be explained by the scattering property of the fibers in that region: since the wavelength is close to the

size of the fibers, scattering becomes dominant. However, the R differences in this wavelength region do not result in a significant difference for the final integrated total reflectance (ρ) value, due to the gradually decreasing nature of the human body emissivity, thus it does not significantly adjust the lower setpoint temperature, and all three configurations lead to an almost equal value of 18 °C. We note that the results of fiber and membrane cases are even more similar for the cooling situation (low particle volume fraction), leading to the same upper setpoint temperature as well.

In light of this, one can utilize the MMDF design based on a membrane, an ordered or a random fiber approach, all leading to a dynamic temperature regulation functionality.

6. Conclusion

In this work, we propose a passive dynamic thermoregulation fabric that capitalizes on the strong scattering properties of metal microspheres and the mechanical and thermal properties of a shape memory polymer. We implement detailed electromagnetic and radiation transport models to study its optical properties. These serve as input for a heat transfer analysis to evaluate the thermal performance of the fabric. Due to a small volume fraction requirement and a lower health risk (due to size and weight), micrometer-sized metal particles possess important advantages over the customary nanoparticles.

Using particles with radius 1.5 μm and a fabric thickness of 150 μm , our design demonstrates a wide setpoint temperature window of 8 °C, delivering thermal comfort in the range of 18–26 °C. Furthermore, a large selection of materials can be envisaged, both for the microspheres and for the matrix. Various environmental and fabric parameters were investigated, showing that the design performs in both heating and cooling modes within flexible parameter ranges. Extreme outdoor environments were not examined, as the main objective is to provide a dynamic fabric for indoor applications, such as offices, where one can control the ambient temperature and air circulation. Furthermore, due to its compatibility with well-established fabrication techniques, large scale manufacturing of the textile seems feasible. Finally, this concept is also useful for other applications in the infrared domain, such as thermal camouflage, IR filters and smart thermal management devices.

Conflicts of interest

There are no conflicts to declare.

Acknowledgements

We acknowledge support from the INTERREG PHOTONITEX project.

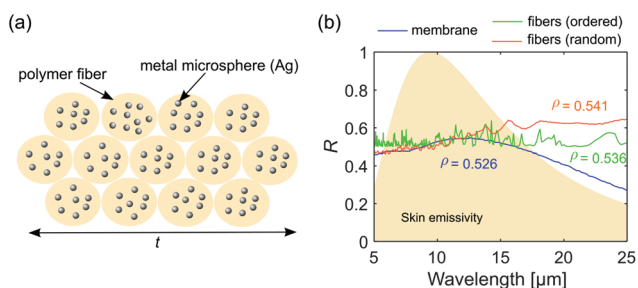


Fig. 5 (a) Schematic illustration of fabric cross section composed of microparticle doped fibers (ordered arrangement), (b) R as a function of wavelength for a fabric design constituted from microparticle ($r = 1.5 \mu\text{m}$) doped fibers with radius $r_f = 15 \mu\text{m}$ oriented randomly (orange) and ordered (green) in comparison with membrane based design (blue), fabric thickness $t = 150 \mu\text{m}$ and particle volume fraction $f_v = 0.05$.

References

- 1 A. J. McMichael, R. E. Woodruff and S. Hales, *Lancet*, 2006, **367**, 859–869.
- 2 G.-R. Walther, E. Post, P. Convey, A. Menzel, C. Parmesan, T. J. Beebee, J.-M. Fromentin, O. Hoegh-Guldberg and F. Bairlein, *Nature*, 2002, **416**, 389.
- 3 J. D. Hardy and E. F. DuBois, *Proc. Natl. Acad. Sci. U. S. A.*, 1937, **23**, 624.
- 4 H. Luo, Q. Li, K. Du, Z. Xu, H. Zhu, D. Liu, L. Cai, P. Ghosh and M. Qiu, *Nano Energy*, 2019, **65**, 103998.
- 5 A. Hazarika, B. K. Deka, D. Kim, H. E. Jeong, Y.-B. Park and H. W. Park, *Nano Lett.*, 2018, **18**, 6731–6739.
- 6 S. Jafar-Zanjani, M. M. Salary and H. Mosallaei, *ACS Photonics*, 2017, **4**, 915–927.
- 7 S. Assaf, M. Boutghatin, Y. Pennec, V. Thomy, A. Korovin, A. Treizebre, M. Carette, A. Akjouj and B. Djafari-Rouhani, *Sci. Rep.*, 2020, **10**, 1–9.
- 8 P. B. Catrysse, A. Y. Song and S. Fan, *ACS Photonics*, 2016, **3**, 2420–2426.
- 9 P.-C. Hsu, A. Y. Song, P. B. Catrysse, C. Liu, Y. Peng, J. Xie, S. Fan and Y. Cui, *Science*, 2016, **353**, 1019–1023.
- 10 Y. Guo, C. Dun, J. Xu, J. Mu, P. Li, L. Gu, C. Hou, C. A. Hewitt, Q. Zhang, Y. Li, *et al.*, *Small*, 2017, **13**, 1702645.
- 11 L. Cai, Y. Peng, J. Xu, C. Zhou, C. Zhou, P. Wu, D. Lin, S. Fan and Y. Cui, *Joule*, 2019, **3**, 1478–1486.
- 12 J. K. Tong, X. Huang, S. V. Boriskina, J. Loomis, Y. Xu and G. Chen, *ACS Photonics*, 2015, **2**, 769–778.
- 13 P.-C. Hsu, X. Liu, C. Liu, X. Xie, H. R. Lee, A. J. Welch, T. Zhao and Y. Cui, *Nano Lett.*, 2015, **15**, 365–371.
- 14 L. Cai, A. Y. Song, P. Wu, P.-C. Hsu, Y. Peng, J. Chen, C. Liu, P. B. Catrysse, Y. Liu, A. Yang, *et al.*, *Nat. Commun.*, 2017, **8**, 1–8.
- 15 K. Wu, L. Yu, C. Lei, J. Huang, D. Liu, Y. Liu, Y. Xie, F. Chen and Q. Fu, *ACS Appl. Mater. Interfaces*, 2019, **11**, 40685–40693.
- 16 E. M. Leung, M. C. Escobar, G. T. Stiubianu, S. R. Jim, A. L. Vyatskikh, Z. Feng, N. Garner, P. Patel, K. L. Naughton, M. Follador, *et al.*, *Nat. Commun.*, 2019, **10**, 1–10.
- 17 X. A. Zhang, S. Yu, B. Xu, M. Li, Z. Peng, Y. Wang, S. Deng, X. Wu, Z. Wu, M. Ouyang, *et al.*, *Science*, 2019, **363**, 619–623.
- 18 P.-C. Hsu, C. Liu, A. Y. Song, Z. Zhang, Y. Peng, J. Xie, K. Liu, C.-L. Wu, P. B. Catrysse, L. Cai, *et al.*, *Sci. Adv.*, 2017, **3**, e1700895.
- 19 M. G. Abebe, G. Rosolen, E. Khoussakoun, J. Odent, J.-M. Raquez, S. Desprez and B. Maes, *Phys. Rev. Appl.*, 2020, **14**, 044030.
- 20 S. Atiganyanun, J. B. Plumley, S. J. Han, K. Hsu, J. Cytrynbaum, T. L. Peng, S. M. Han and S. E. Han, *ACS Photonics*, 2018, **5**, 1181–1187.
- 21 H. H. Kim, E. Im and S. Lee, *Langmuir*, 2020, **36**, 6589–6596.
- 22 Y. Zhai, Y. Ma, S. N. David, D. Zhao, R. Lou, G. Tan, R. Yang and X. Yin, *Science*, 2017, **355**, 1062–1066.
- 23 L. Cai, A. Y. Song, W. Li, P.-C. Hsu, D. Lin, P. B. Catrysse, Y. Liu, Y. Peng, J. Chen, H. Wang, *et al.*, *Adv. Mater.*, 2018, **30**, 1802152.
- 24 M. Boutghatin, S. Assaf, Y. Pennec, M. Carette, V. Thomy, A. Akjouj and B. Djafari-Rouhani, *Nanomaterials*, 2020, **10**, 1968.
- 25 F. Pilate, A. Toncheva, P. Dubois and J.-M. Raquez, *Eur. Polym. J.*, 2016, **80**, 268–294.
- 26 J.-M. Raquez, S. Vanderstappen, F. Meyer, P. Verge, M. Alexandre, J.-M. Thomassin, C. Jérôme and P. Dubois, *Chem. – Eur. J.*, 2011, **17**, 10135–10143.
- 27 T. Defize, R. Riva, J.-M. Raquez, P. Dubois, C. Jérôme and M. Alexandre, *Macromol. Rapid Commun.*, 2011, **32**, 1264–1269.
- 28 A. Lendlein and O. E. Gould, *Nat. Rev. Mater.*, 2019, **4**, 116–133.
- 29 M. F. Modest, *Radiative heat transfer*, Academic press, 2013.
- 30 M. I. Mishchenko, *OSA Continuum*, 2018, **1**, 243–260.
- 31 L. A. Dombrovskii, *Teplofiz. Vys. Temp.*, 2004, **42**, 772–779.
- 32 L. Dombrovsky, *High Temp.*, 2005, **43**, 247–258.
- 33 W. Mundy, J. Roux and A. Smith, *J. Opt. Soc. Am.*, 1974, **64**, 1593–1597.
- 34 H. U. Yang, J. D’Archangel, M. L. Sundheimer, E. Tucker, G. D. Boreman and M. B. Raschke, *Phys. Rev. B: Condens. Matter Mater. Phys.*, 2015, **91**, 235137.
- 35 J. Beattie, *Physica*, 1957, **23**, 898–902.
- 36 L. Dombrovskii and V. Mironov, *J. Commun. Technol. Electron.*, 1997, **42**, 492–496.
- 37 J. R. Howell, M. P. Mengüç, K. Daun and R. Siegel, *Thermal radiation heat transfer*, CRC press, 2020.
- 38 R. A. Yalçın, E. Blandre, K. Joulain and J. Dré villon, *ACS Photonics*, 2020, **7**, 1312–1322.
- 39 R. A. Yalçın, E. Blandre, K. Joulain and J. Dré villon, *Sol. Energy Mater. Sol. Cells*, 2020, **206**, 110320.
- 40 F. Retailleau, V. Allheily, L. Merlat, J.-F. Henry and J. Randrianalisoa, *J. Quant. Spectrosc. Radiat. Transfer*, 2020, 107300.
- 41 L. G. Henyey and J. L. Greenstein, *Astrophys. J.*, 1941, **93**, 70–83.
- 42 V. A. Markel, *J. Opt. Soc. Am. A*, 2016, **33**, 1244–1256.
- 43 J. Steketee, *Phys. Med. Biol.*, 1973, **18**, 686.
- 44 D. Ding, T. Tang, G. Song and A. McDonald, *Text. Res. J.*, 2011, **81**, 398–411.
- 45 D. Hasselman and L. F. Johnson, *J. Compos. Mater.*, 1987, **21**, 508–515.
- 46 J. Ordóñez-Miranda, R. Yang and J. Alvarado-Gil, *J. Appl. Phys.*, 2012, **111**, 044319.
- 47 B. W. Olesen, *Tech. Rev.*, 1982, **2**, 3–37.
- 48 B. W. Olesen and K. Parsons, *Energy Build.*, 2002, **34**, 537–548.
- 49 D. Zhang, Y. Liu, K. Yu and J. Leng, *J. Intell. Mater. Syst. Struct.*, 2011, **22**, 2147–2154.
- 50 R. Beblo, K. Gross and L. Mauck Weiland, *J. Intell. Mater. Syst. Struct.*, 2010, **21**, 677–683.
- 51 F. Xie, L. Huang, Y. Liu and J. Leng, *Polymer*, 2014, **55**, 5873–5879.
- 52 K. Wang, G. Zhu, Y. Wang and F. Ren, *J. Appl. Polym. Sci.*, 2015, **132**, 42045.

- 53 S. Shi, Q.-Y. Wu, L. Gu, K. Zhang and H. Yu, *RSC Adv.*, 2016, **6**, 79268–79274.
- 54 L. Shuai, Z. Jun, C. Jianjun, Y. Ming, L. Xuepeng and J. Zhiguo, *Polym. Eng. Sci.*, 2019, **59**, E310–E316.
- 55 J. Leng, X. Wu and Y. Liu, *J. Appl. Polym. Sci.*, 2009, **114**, 2455–2460.
- 56 C.-L. Zhang, F.-H. Cao, J.-L. Wang, Z.-L. Yu, J. Ge, Y. Lu, Z.-H. Wang and S.-H. Yu, *ACS Appl. Mater. Interfaces*, 2017, **9**, 24857–24863.
- 57 X.-H. Li, C. Liu, S.-P. Feng and N. X. Fang, *Joule*, 2019, **3**, 290–302.
- 58 S. Karakus, E. Tan, M. Ilgar, I. S. Basdemir and A. Kilislioglu, *New Trends in Ion Exchange Studies*, IntechOpen, 2018, pp. 1–14.
- 59 Q. Liu, J. Huang, J. Zhang, Y. Hong, Y. Wan, Q. Wang, M. Gong, Z. Wu and C. F. Guo, *ACS Appl. Mater. Interfaces*, 2018, **10**, 2026–2032.
- 60 F. Gao, *Advances in polymer nanocomposites: types and applications*, Elsevier, 2012.
- 61 R. M. Mutiso and K. I. Winey, *Prog. Polym. Sci.*, 2015, **40**, 63–84.
- 62 F. Faupel, V. Zaporojtchenko, T. Strunskus and M. Elbahri, *Adv. Eng. Mater.*, 2010, **12**, 1177–1190.
- 63 Q. Yang, T. Wang, L. Zhang, J. Zhang, F. Wang, Y. Ni, S. Pan, Y. Li and J. You, *Appl. Surf. Sci.*, 2019, **480**, 276–280.
- 64 J. A. Galloway, K. J. Koester, B. J. Paasch and C. W. Macosko, *Polymer*, 2004, **45**, 423–428.
- 65 W. Feng, Y.-s. Zhang, Y.-w. Shao, T. Huang, N. Zhang, J.-h. Yang, X.-d. Qi and Y. Wang, *Eur. Polym. J.*, 2021, **145**, 110245.
- 66 Y. Jia, X. Yue, Y. Wang, C. Yan, G. Zheng, K. Dai, C. Liu and C. Shen, *Composites, Part B*, 2020, **183**, 107696.
- 67 Y. Peng, J. Chen, A. Y. Song, P. B. Catrysse, P.-C. Hsu, L. Cai, B. Liu, Y. Zhu, G. Zhou, D. S. Wu, *et al.*, *Nat. Sustain.*, 2018, **1**, 105–112.
- 68 Y. Battie, A. Resano-Garcia, N. Chaoui, Y. Zhang and A. En Naciri, *J. Chem. Phys.*, 2014, **140**, 044705.
- 69 R. G. Barrera and A. Garcia-Valenzuela, *J. Opt. Soc. Am. A*, 2003, **20**, 296–311.
- 70 X. Wu, L. Yuan, X. Weng, L. Qi, B. Wei and W. He, *Nano Lett.*, 2021, **21**, 3908–3914.